Author(s): Niemi, Tero J. & Guillaume, Joseph H. A. & Kokkonen, Teemu & Hoang, Tam M. T. & Seed, Alan W.

Title: Role of spatial anisotropy in design storm generation: Experiment and interpretation

Year: 2015

Version: Final published version

AGU PUBLICATIONS

Water Resources Research

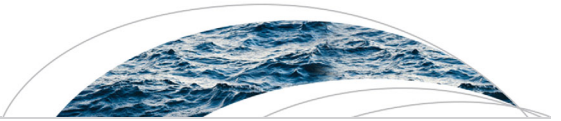

RESEARCH ARTICLE

10.1002/2015WR017521

Role of spatial anisotropy in design storm generation: Experiment and interpretation

Tero J. Niemi[1], Joseph H. A. Guillaume[1], Teemu Kokkonen[1], Tam M. T. Hoang[2], and Alan W. Seed[3]

[1]Department of Civil and Environmental Engineering, School of Engineering, Aalto University, Espoo, Finland, [2]Hydrology and Flood Warning, Melbourne Water, Melbourne, Victoria, Australia, [3]Centre for Australian Weather and Climate Research, Bureau of Meteorology, Melbourne, Victoria, Australia

Key Points:
- Method to produce design storms with anisotropic spatial shape is presented
- Method allows for realistic description of rainband features at large scale
- Anisotropy had small impact on runoff after controlling for rainfall amount

Supporting Information:
- Supporting Information S1
- Movie S1
- Movie S2
- Movie S3

Correspondence to:
T. J. Niemi,
tero.niemi@aalto.fi

Citation:
Niemi, T. J., J. H. A. Guillaume, T. Kokkonen, T. M. T. Hoang, and A. W. Seed (2015), Role of spatial anisotropy in design storm generation: Experiment and interpretation, *Water Resour. Res.*, *51*, doi:10.1002/2015WR017521.

Received 12 MAY 2015
Accepted 9 DEC 2015
Accepted article online 16 DEC 2015

Abstract Rainfall accumulation depths over a given area are strongly dependent on the shape of the storm together with its direction of advection. A method to produce design storms exhibiting anisotropic spatial scaling is presented by combining a state-of-the-art stochastic rainfall generator STEPS with the linear generalized scale invariance (GSI) notation. The enhanced model is used to create ensembles of design storms based on an extreme storm with a distinct rainband shape observed in Melbourne, Australia. Design storms are generated both with and without accounting for anisotropy. Effect of anisotropy on precipitation characteristics is studied using the entire region covered by the radar (*radar scale*) and at a significantly smaller *catchment scale*. A rainfall-runoff model is applied to route the rainfall through the catchment into streamflow. Accounting for anisotropy allows for a more realistic description of precipitation features at the radar scale. At the catchment scale, anisotropy increases the probability of high rainfall accumulations, which translates into greater flood volumes. No discernible difference was observed in streamflow characteristics after controlling for the accumulation over the catchment. This could be explained by a lower importance of anisotropy relative to other factors affecting streamflow generation, and by the difficulties in creating representative rainfall temporal properties at the catchment scale when the radar scale is used for model calibration. The proposed method provides a tool to create ensembles of design storms when the anisotropic shape of the fields is of importance.

1. Introduction

Design storms are often required for designing engineering works, such as urban drainage systems and dams. For hydrological studies, they are often generated using simulation models due to the convenience of easily controlling the model parameters. Combined with rainfall-runoff models, they can be used to estimate the quantities of interest at a given point in the catchment. Notably, design storms consisting of stochastic precipitation fields have been extensively used to investigate the catchment response to storm properties, be it in a fully urban context [e.g., *Gires et al*., 2012] or with catchments of a more natural state [e.g., *Gabellani et al*., 2007; *Volpi et al*., 2012; *Paschalis et al*., 2014].

Precipitation generators based on random fields are attractive, as they are capable of producing simulations exhibiting scaling behavior with realistic spatiotemporal statistics at high resolutions in space and time. However, the majority of the available models relying on scaling random fields are designed to create fields consisting of only isotropic rain features [e.g., *Bell*, 1987; *Pegram and Clothier*, 2001; *Rebora et al*., 2006; *Paschalis et al*., 2013]. This is typically motivated by assuming an isotropic model to be a reasonable approximation for most practical needs. However, real precipitation fields often exhibit anisotropic characteristics even at the mesoscale where the simulation models are commonly applied. This anisotropic nature can be attributed to e.g., orographic forcing [*Ebtehaj and Foufoula-Georgiou*, 2010] or to frontal squall lines, as in the storm examined in this study.

The anisotropic spatial structure of a storm and the direction of its advection have a major role in controlling the amount of accumulated precipitation falling over a given area. Consider three cases in which a storm has the same intensity, velocity, and direction of movement: (1) an elongated storm (e.g., a squall line) with the motion vector normal to the elongation, (2) an isotropic storm with an approximately round shape, and (3) an elongated storm with the motion vector parallel to the elongation. These storms will

produce increasing accumulations over the catchment due to the different rain durations associated with the systems. Assuming that the storms are similar except for their shape, the differences in the durations and hence in the accumulated rainfalls result solely from the structure of the precipitating features of the storm in relation to the advection.

Anisotropic precipitation structures have previously been simulated using a variety of approaches. These include methods based on point processes [e.g., *Waymire et al*., 1984; *Mellor*, 1996; *Northrop*, 1998], spectral techniques with different scaling exponents to orthogonal directions [*De Michele and Bernardara*, 2005], and geostatistics [e.g., *Vischel et al*., 2009; *Leblois and Creutin*, 2013; *Schleiss et al*., 2014]. The Generalized Scale Invariance (GSI) and universal multifractals are a particularly promising approach. *Pecknold et al*. [1993] used this approach on static fields, without considering temporal development of those fields. *Marsan et al*. [1996] provide tools to develop full space-time rainfall simulations utilizing the anisotropic multifractal fields, however, applications using the method have been scarce and the tools are not currently available in commonly used precipitation generators.

In this study, design storms are created with realistic spatial and temporal properties and an elongated, rainband-like shape, using a state-of-the-art precipitation generator STEPS [*Bowler et al*., 2006; *Seed et al*., 2013] combined with the linear Generalized Scale Invariance (GSI) formalism [*Schertzer and Lovejoy*, 1985]. While this combination is just one alternative to introduce anisotropy to an otherwise isotropic model, it is appealing, as STEPS is based on the assumption of scaling precipitation fields and GSI simply provides a tool for extension from isotropic to anisotropic scaling. To the authors' knowledge, this is the first attempt to incorporate anisotropic spatial scaling to an existing and widely used precipitation generator, providing a new tool to account for anisotropic structures in precipitation fields. The proposed extension of a spatially isotropic model to handle anisotropic fields is not tied to STEPS, however, but should be a viable option for other simulation models relying on scaling random fields as well, e.g., the aforementioned models of *Bell* [1987], *Pegram and Clothier* [2001], and *Paschalis et al*. [2013].

In this paper, two ensembles of design storms are stochastically generated using the extended STEPS model. They are parameterized using an observed extreme event exhibiting a distinct rainband structure. One ensemble accounts for the spatial anisotropy in the observed event, whereas the other omits the anisotropic characteristics. The precipitation ensembles are analyzed and compared against each other at two spatial scales: the *radar scale* covering a square of 256×256 km^2 and the considerably smaller *catchment scale* ($\sim 1\,100$ km^2). Finally, both ensembles are used to drive a semidistributed rainfall-runoff model URBS [*Carroll*, 1998], and the resulting streamflow hydrographs are compared at the catchment outlet.

The aim of the analysis is to identify differences between isotropic and anisotropic ensembles representing the same storm event. Notably, the objective is not to compare the simulation results against the measured event, as it is considered here as merely a single realization of a stochastic process. The storm event is, however, an interesting "limit" case with the elongation of the rainband almost parallel to the motion vector. This underlines the role of describing the anisotropic characteristics of the storm, and presumably leads to greater differences in storm and streamflow properties between isotropic and anisotropic ensembles.

This paper is organized as follows. Section 2 presents the observed precipitation event used as a basis for the design storm generation and describes the study area. Section 3 gives a brief description of the models used in this research and outlines the process of implementing GSI in STEPS. Section 4 describes the analyses performed on the simulated ensembles. The results are given and discussed in section 5, and the conclusions of the research are presented in section 6.

2. Data

2.1. Weather Radar Observations

The 43 h event used to parameterize the design storms studied here took place 3–5 February 2011, and was one of the most intense ever observed in the Melbourne Metropolitan area in Victoria, Australia. The storm resulted in exceptionally high daily rainfall totals in numerous locations, including daily rainfall exceeding 150 mm in parts of the study area on 5 February. It was caused by repeated severe thunderstorms that developed as tropical moisture from post-tropical cyclone Yasi and the remnants of tropical cyclone Anthony interacted with a cold front. The catchments were already saturated by rain events in

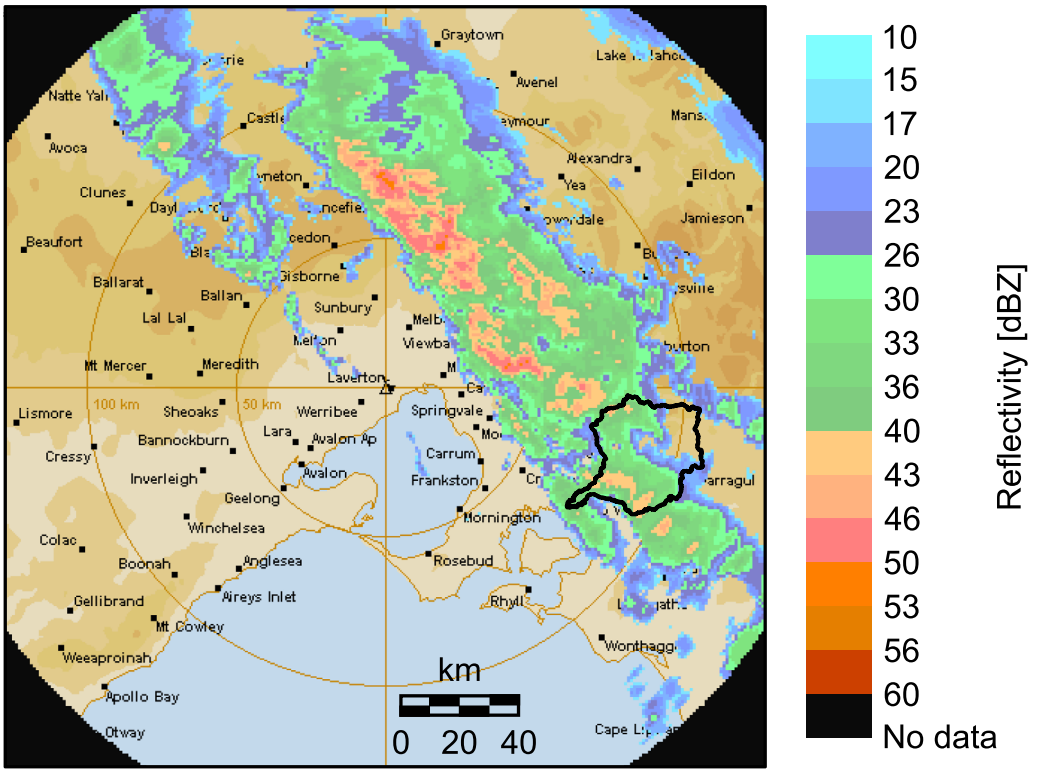

Figure 1. Radar reflectivity field at 4 February 2011 21:30 UTC. The location of the Bunyip River catchment is outlined.

December and January, so the heavy rain resulted in widespread flooding in many Victorian rivers, including the Bunyip River, which is the focus of this research. One of the main causes of the exceptionally high rainfall depths over the study area was the spatial structure of the event combined with the movement of the storm. The squall lines produced by the thunderstorms had an elongated shape almost parallel to the general advection direction of the storm from NW to SE, and many of the squall lines moved directly over the studied catchment, resulting in long and continuous periods of high intensity rain.

The precipitation event was recorded by the Australian Bureau of Meteorology weather radar near Melbourne, Victoria. Preprocessed radar reflectivity (dBZ) fields from the radar were made available with a temporal resolution of 6 min and a spatial resolution of 1 km covering a 256 by 256 km^2 square centered at the radar. An example radar reflectivity field demonstrating the anisotropy of the event is presented in Figure 1 with the location of the study area, the Bunyip River catchment. An animation of the event is available in supporting information. As explained above, this research did not require direct comparison with the actual ground level precipitation measurements or river flows. Therefore, the reflectivity fields were assumed to be free of errors representing the rain features at the ground level, and no observed flow records from the Bunyip River were used.

2.2. Study Area

The 1094 km^2 Bunyip River catchment (Figure 2) is located approximately 60 km southeast of Melbourne. The catchment has a temperate oceanic climate with the mean annual rainfall of 1021 mm ranging from 1600 mm in the north to 800 mm in the south of the catchment. The annual accumulated rainfall is strongly correlated with topography, the elevation ranging from 883 m above sea level in the north to close to sea level in the south of the catchment. The 114 km long Bunyip River originates from the Bunyip State Park in the northern parts of the catchment. The headwaters of its major tributary, the Tarago River, are in the Tarago State Forest from where the river flows into the Tarago reservoir before converging with the Bunyip River. The catchment is characterized by forested natural areas in the upstream parts and rural areas with small townships in the lower parts of the catchment. In the lower parts, many creeks are modified to be

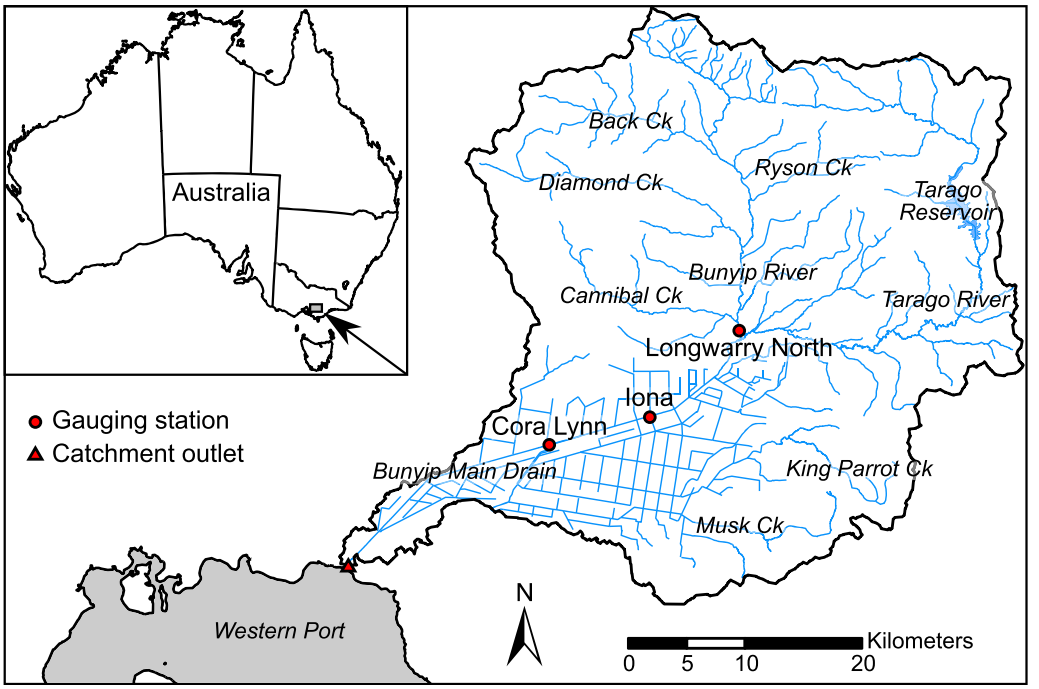

Figure 2. The Bunyip River catchment. Red circles refer to water level gauges in the river. The red triangle depicts the catchment outlet.

agricultural drains, and the Bunyip River is straightened and converted into the Bunyip Main Drain to protect the low-lying areas against flooding. The impervious coverage of the catchment is approximately 3%.

3. Methods

3.1. Stochastic Rainfall Generator (STEPS)

The ensembles of stochastic precipitation events are generated using a multiplicative cascade-based simulation model STEPS [*Bowler et al*., 2006]. The model relies on the long-known notion that precipitation fields exhibit spatial scaling behavior consistent with multifractality [*Veneziano et al*., 2006] and dynamic scaling [*Venugopal et al*., 1999], the latter of which relates lifetime of the structures to their size. The model was developed as a precipitation nowcasting system to merge an extrapolation nowcast with a downscaled numerical weather-prediction forecast. However, it can also be used in a parametric mode to create purely stochastic simulations of precipitation events. As the details of the current state of the model are given in *Seed et al*. [2013], only a brief description of the model is presented here. For more details, the reader is referred to the previous publications and references therein. The input parameters of the model, and animations of anisotropic and isotropic simulations are provided in supporting information.

Using STEPS in the parametric mode involves first generating time series for the mean areal rainfall over the entire field, $R(t)$, and the field advection velocities to eastern, $E(t)$, and southern, $S(t)$, directions using the broken line model of *Seed et al*. [2000]. For each time step, the spatial scaling structure of a precipitation field is approximated by filtering a field of white noise with power law filters in the Fourier domain to replicate the average spectral density, or the power spectrum, of a given rainfall event. The exponents of the power law filters are related to $R(t)$ using quadratic functions. The spatially correlated noise field is then decomposed into cascade levels using a set of Gaussian band-pass filters corresponding to different spatial scales.

The Lagrangian temporal evolution of the field is accomplished by modeling the lifetimes of the cascade levels as second-order autoregressive AR(2) processes, and assuming that the temporal autocorrelations follow a power law that relates the temporal correlation length to the spatial scale. Advection is described by moving pixels at each cascade level for the two preceding time steps (lag-1 and lag-2 terms) to eastern and

southern directions according to advection velocities $E(t)$ and $S(t)$, respectively. The current noise field represents the innovation term in the AR-model. The advected and temporally updated cascade level fields are finally recomposed back to a single noise field.

In order to ensure smooth advection handling and spatially continuous features when crossing the field edges, the advection scheme of *Pegram and Clothier* [2001] was in this research implemented to STEPS by utilizing the "wrap-around" property of the Fourier transform. Therefore, noise fields having the size of $2L \times 2L$ were generated where the rain features seemingly continue from one side of the field to another, and the advection is simulated by moving a slice of the field from one side of the field to another side. After recomposition, the fields are trimmed to the final size of $L \times L$ by only using the central part of the field.

The final precipitation field at time t is obtained by adjusting the field wetted area ratio $WAR(t)$, field mean $R(t)$, and field standard deviation $\sigma(t)$. $WAR(t)$, describing the proportion of wet pixels in a precipitation field, and $\sigma(t)$ were related to $R(t)$ using quadratic functions as these two properties were detected to be strongly correlated with $R(t)$ ($p > 0.95$). In simulations, the values of the recomposed field below some threshold are set to zero to obtain the correct $WAR(t)$, as calculated from $R(t)$. Since setting $WAR(t)$ alters the field mean and standard deviation, the thresholded field must still be scaled and shifted to correct $R(t)$ and $\sigma(t)$.

Despite the relatively large precipitation gradient in the annual rainfall amounts due to the elevation differences between northern and southern parts of the catchment, the orographic enhancement was not taken into account in simulations, as it was noticed to be negligible in the case of an individual storm event.

3.2. Generalized Scale Invariance (GSI)

The fields generated with STEPS are scale invariant, i.e., the field observed at a given scale is statistically similar to the field observed at a different scale. As the generated precipitation features exhibit no preferred orientation in space, the scaling is isotropic. For a field to be scale invariant its spatial power spectrum, P_s, needs to have a power law form:

$$P_s(\omega) \sim \omega^{-\beta} \tag{1}$$

where ω is the frequency in Fourier domain and β is the power spectrum exponent. For two-dimensional (2-D) fields, the Fast Fourier Transform (FFT) can be used to conveniently calculate a 2-D power spectrum $P_s(\boldsymbol{\omega}) = P_s(\omega_x, \omega_y)$ which is then radially averaged about $\omega_x = \omega_y = 0$ to obtain $P_s(\omega)$, where $\omega = |\boldsymbol{\omega}| = \sqrt{\omega_x^2 + \omega_y^2}$. A family of nested contour lines can be drawn on the 2-D P_s. In the isotropic case, the contours are circles, each of which represents one spatial scale in the field. The field at a given scale is simply a magnified version of the field at another scale.

To create features exhibiting anisotropic scaling, the magnification or reduction between scales has to be accompanied with stretching and rotation. GSI [*Schertzer and Lovejoy*, 1985] is a general tool for describing anisotropic scaling in geophysical systems. Only a brief description of the key concepts of GSI are given here, and for a more complete description the reader is referred to e.g., *Lovejoy and Schertzer* [2013].

In GSI, a scale changing operator, T_λ, relates the statistical properties at one scale to another scale, so that these properties are a function of only the ratio λ between the scales:

$$T_\lambda = \lambda^{-\mathrm{G}} \tag{2}$$

where G is the generator defining the transformation between the scales. Here the consideration is restricted to linear GSI where the anisotropy is assumed to be statistically homogenous, i.e., independent of the location in the field. In linear GSI, T_λ is a linear transformation and the generator G is described by a single matrix.

As with isotropic scaling, the contours of the 2-D P_s of an anisotropic field represent the individual scales of the field, but now the contours can have any shape as long as they do not cross each other. In the prevailing GSI literature, the objects representing different scales of the field are traditionally referred to as "balls," B, even though they are in fact two-dimensional objects for 2-D fields. The same notation and terminology is adopted here. Now, the contours of the 2-D power spectrum can be taken as a family of balls covering the entire field.

GSI requires that one of the contours is selected as the unit ball, B_1, from which other balls are calculated. Here it is assumed that there exists a scale, the "sphero-scale," where the precipitation features are approximately isotropic. This is often the case with smaller structures of precipitation fields despite large structures often being anisotropic [*Zawadzki*, 1973; *Kumar and Foufoula-Georgiou*, 1993; *Niemi et al.*, 2014]. The unit ball corresponding to the sphero-scale is a circle, defined by the frequency corresponding to its radius in Fourier space, l_s. Consequently, all the non-unit balls, B_λ, can be obtained from:

$$B_\lambda = \tilde{T}_\lambda B_1, \tag{3}$$

where $\tilde{T}_\lambda = \lambda^{-\tilde{G}} = \lambda^{-G^T}$ is the Fourier space scaling operator corresponding to T_λ [*Pflug et al.*, 1993]. Since B_1 is a circle, the family of balls obtained from acting on it with $\tilde{T}_\lambda$ are stretched and rotated ellipses. The entire anisotropic system is now parameterized by the generator G and the size of the sphero-scale l_s.

In 2-D linear GSI, the generator G is a 2×2 matrix with four parameters controlling the anisotropy of the system through rotation (*e*), stretching (*c* and *f*), and overall contraction (*d*) of scales [*Schertzer and Lovejoy*, 1985]:

$$G = \begin{bmatrix} d+c & f-e \\ f+e & d-c \end{bmatrix}. \tag{4}$$

Following *Lovejoy and Schertzer* [2013], the parameters controlling stretching can be combined as

$$r = \sqrt{c^2+f^2} \tag{5}$$

and to facilitate simulations it suffices to consider the characteristics of G independent of the absolute orientation by setting $c = 0$. Furthermore, in 2-D the overall contraction parameter d can be always taken as $d = 1$, which yields the generator in a coordinate system that needs to be rotated by angle θ to attain the correct orientation for the system:

$$G' = \begin{bmatrix} 1 & r-e \\ r+e & 1 \end{bmatrix}. \tag{6}$$

The coordinate systems between G and G′ are related by

$$G = \Omega^{-1} G' \Omega, \tag{7}$$

where Ω is the rotation matrix $\Omega = \begin{bmatrix} \cos(\theta) & -\sin(\theta) \\ \sin(\theta) & \cos(\theta) \end{bmatrix}$. Using equation (7) θ and r can now be related to parameters c and f:

$$c = r \sin(2\theta) \tag{8a}$$

$$f = r \cos(2\theta) \tag{8b}$$

Creating anisotropic structures therefore requires producing time series for the extent of stretching of the system (r), the rotation between scales (e), and the overall rotation of the system (θ). While in model calibration c and f are estimated directly according to *Niemi et al.* [2014], for simulations, it is preferable to use r and θ, as the extent and the orientation of anisotropy can be controlled separately instead of controlling both variables simultaneously.

3.3. Integration of GSI and STEPS

Incorporating GSI into STEPS requires changes to the power law filter and the band-pass filters. As noted in section 3.1, to generate the desired isotropic spatial structure for the simulated rainfall field, STEPS filters a field of white noise using a two-part power law filter of the following form [*Seed et al.*, 2013]:

$$f(\omega) = \left(\frac{\omega}{\omega_0}\right)^{-\frac{\beta_1}{2}} \text{for } \omega \le \omega_b, \tag{9a}$$

$$f(\omega)=f(\omega_b)\left(\frac{\omega}{\omega_b}\right)^{-\frac{\beta_2}{2}} \text{ for } \omega > \omega_b, \tag{9b}$$

where the target field has horizontal dimensions of L by L pixels, $\omega_0=1/L$, ω_b is the scaling break where the slope of the power law changes, and β_1 and β_2 are the slopes of the power spectrum at frequencies below and above ω_b, respectively. While the exact multifractality of the model is disrupted by the introduced scale break, the assumption of different scaling exponents for large and small scales is supported by empirical observations in literature [*Seed et al*., 2013; *Willeit et al*., 2015] and by the data used here (not shown). Furthermore, as required by linear GSI, it is assumed here that the scale break does not affect the GSI matrix G, but that the same matrix is valid for the entire field. The anisotropic simulations obtained (section 5.2) suggest that this simplifying assumption provides acceptable results.

For anisotropic simulations, the frequencies $\omega=|\boldsymbol{\omega}|=\sqrt{\omega_x^2+\omega_y^2}$ cannot be used in the power law filter as in equation (9), since the balls describing the scales of an anisotropic field are not circles. Instead, in the anisotropic case, the frequencies ω have to be replaced with ω_λ obtained from:

$$\boldsymbol{\omega}_\lambda=\tilde{T}_\lambda\boldsymbol{\omega}_1, \tag{10}$$

where $\boldsymbol{\omega}_1$ lies on the unit circle. Equation (10) has to be solved for every location (ω_x,ω_y) in the frequency field. The frontier of the ball B_λ on scale λ is defined by $\boldsymbol{\omega}_\lambda$, which describes all the locations (ω_x,ω_y) in the field sharing the same value of ω_λ. The detailed procedure for calculating ω_λ is presented in *Pecknold et al*. [1993].

In addition to the power law filter, STEPS uses band-pass filters to decompose the correlated noise fields into cascade levels. For isotropic simulations, the kth level in the cascade represents the variability in the simulation field with frequencies, ω_k, in the range $(q^{k-1})/L < \omega_k < (q^k)/L$, where q is the cascade scale ratio between levels $k-1$ and k [*Seed et al*., 2013]. For anisotropic simulations, the band-pass filters have to be defined in terms of $\omega_{\lambda,k}$ to account for the anisotropic scaling.

3.4. Calibration of STEPS

A two-step procedure was used to calibrate STEPS for anisotropic and isotropic simulations. In the first step, the parameters were estimated directly from the observed successive radar reflectivity fields. In the second step, the parameters were fine-tuned for best performance for both model instances by comparing the observed storm with ensembles of simulated anisotropic and isotropic storms.

The sequence of observed radar reflectivity fields was used to obtain time series for the mean areal rainfall, field standard deviation, and field wetted area ratio of the observed event. The advection velocity time series toward the east and south directions were estimated from a sequence of observed reflectivity fields using the optical flow algorithm of *Bowler et al*. [2004].

$\sigma(t)$ and *WAR*(t) were parameterized by fitting quadratic functions between the values of the observed mean areal rainfall and both the field standard deviation and the field wetted area ratio. A radially averaged spatial power spectrum according to equation (1) was estimated for each observed field, and the slopes above and below the scaling break (18 km) were also related to the mean areal rainfall using quadratic functions to obtain values for power law filter parameters $\beta_1(t)$ and $\beta_2(t)$. The observed time series of mean areal rainfall and advection velocities were used to determine parameters for the broken line models describing *R*(t), *E*(t), and *S*(t), following the methods described in *Seed et al*. [2000] and *Seed et al*. [2014].

The observed reflectivity fields were decomposed according to the spatial scale into cascade levels using FFT and band-pass filtering, and the lag-1 and lag-2 autocorrelations between consecutive reflectivity fields were estimated for each level. The average autocorrelations at each level were used to relate spatial and temporal scaling using a power law equation. Further details on parameterizing STEPS for simulating stochastic precipitation fields are given in *Seed et al*. [2014].

The spatial anisotropy of the observed event was estimated using the method of *Niemi et al*. [2014] by identifying the time series of the GSI parameters best fitting isolines of constant power on the two-dimensional power spectrum of the fields. The sphero-scale was found to be located near the smallest scales throughout the event. As suggested by *Niemi et al*. [2014], it was therefore assumed to be constant at 2 km to reduce the computational burden of the method. The rotation between scales was considered to be of minor

importance in comparison to the overall anisotropy of the precipitation features, given that the dominant rainfall structures were mesoscale rainbands having a relatively distinct elongated shape. Therefore, to further streamline the parameter estimation and to simplify the simulations, it was assumed that there was no rotation between the scales ($e = 0$). Thus, it was sufficient to identify GSI generator parameters c and f for each field. These were then converted to time series describing the extent of stretching (r) and the overall rotation (θ) of the observed event, using equations (5) and (8).

For anisotropic simulations, the time series describing the extent of anisotropy in the observed event was used to parameterize the broken line model applied in generating the r values. θ, however, was kept constant at $\theta = 112.5°$ to simplify the simulation process. For isotropic simulations $r = 0$, causing e, θ, and l_s to become irrelevant. Reducing the parameter space by keeping e and l_s constant forces the remaining parameters, c and f, to compensate for the effect of the eliminated parameters. However, independent estimates of all parameters confirmed the effect of e and l_s on the estimates of r and θ to be of minor significance (see section 4.3 and Figure 5 in section 5.2).

After establishing the initial parameter estimates for STEPS, the anisotropic and isotropic models were used to create ensembles of design storms. The model parameters were then manually adjusted to get the best performance for both models by comparing the simulated ensembles to the observed event. In comparison with the observed event and the anisotropic model, the isotropic model produced too low hourly and 3 hourly point accumulations, as well as too low values of the Eulerian autocorrelation function for instantaneous fields and hourly accumulation fields at the pixel resolution. This was to be expected, considering that the prevailing anisotropy of the fields was almost parallel to the advection direction. To produce the same point accumulation, an isotropic storm either has to have a higher intensity or a slower velocity than the corresponding anisotropic storm. This compensates for the longer time the elongated storm takes while travelling over a given point. The advection velocity of the isotropic model was therefore decreased, and slight adjustments were made to the parameters of the AR(2) model.

Results of the model calibration are evaluated in section 5.1.

3.5. Rainfall-Runoff Model

URBS [*Carroll*, 1998] is a semidistributed runoff routing model developed primarily for flood forecasting and design flood assessments. The model has been used in several case studies across Australia [e.g., *Rahman et al*., 2007; *Charalambous et al*., 2013] and it is in operational use for flood forecasting throughout Australia, including the Bunyip River catchment.

In URBS, a catchment is divided into several subareas and the total rainfall is determined over each subarea. Catchment losses are characterized for each of the subareas using an initial loss followed by either a "proportional loss" or a "continuing loss." Subareal rainfalls and the estimated losses together yield the excess rainfall. The excess rainfall is converted to runoff and separated into catchment and channel routing for obtaining streamflow hydrographs at given locations.

Melbourne Water operates an URBS model of the Bunyip River catchment where the catchment is divided into 56 subareas with an average size of 19.5 km^2. For operational use, the model parameters have been estimated and verified using a number of major rainfall-runoff events recorded over the catchment from 1996 to 2010 (T. Hoang, URBS FLOOD FORECASTING MODEL, Bunyip River Catchment to Western Port Bay, unpublished report, Melbourne Water, Melbourne, Australia, 2010). For simulations, the key model parameters controlling channel storage, catchment storage, maximum soil storage capacity, initial loss recovery, daily soil storage recovery, and proportion of runoff from nonsaturated areas have been set uniform for the entire catchment. The parameters have been optimized using the PEST software [*Doherty*, 2010] and continuous rainfall-runoff data from 2009 to 2013 at Longwarry North, Iona, and Cora Lynn gauging stations (Figure 2) (D. Carroll, Continuous Simulation Modeling using the URBS model: Bunyip Creek, unpublished report, Melbourne Water, Melbourne, Australia, 2013).

4. Analysis of Simulations

Performance of the anisotropic and isotropic STEPS implementations was first evaluated over the entire 256 by 256 km^2 radar field (*radar scale*) before examining the effects of the anisotropy to the precipitation and

streamflow properties over a region having the size of the Bunyip River catchment (*catchment scale*). The following subsections describe the methods used for these analyses.

4.1. Generation of Ensembles

Two ensembles with 1000 members of stochastic design storms each were generated using STEPS to represent the anisotropic and isotropic reproductions of the observed event. The model parameters used in simulations can be found in supporting information. The extent of the fields and the spatial and temporal resolutions were kept identical to the observed reflectivity fields. Simulated reflectivity fields were converted to rain rates using a Z-R relationship calibrated for the Melbourne radar.

4.2. Evaluation of Model Calibration

The model performance in creating representative design storms was evaluated by comparing the ensemble average spatial scaling properties, the ensemble average temporal scaling properties, and the advection velocities of the generated storms to the properties of the observed storm at the radar scale. In addition, to verify that the shape of the fields does not affect the mean field accumulation, the Kolmogorov-Smirnov test and the two-sample *t* test were used to test the probability distributions of the mean field accumulations of the anisotropic and isotropic models.

4.3. Evaluation of Anisotropy Simulation

The skill of the model at generating fields with an elongated shape was evaluated by comparing the anisotropy of the observed event to the events generated by the anisotropic and isotropic models. The GSI parameters describing the event anisotropy were estimated using the method of *Niemi et al*. [2014] for 100 members from each ensemble to give an indication of stochastic variation between generated fields. Recall that the anisotropic ensemble was generated (1) by assuming the smallest structures to be isotropic ($l_s = 2$ km), (2) allowing only the extent of stretching of the system (r) vary in time while keeping the orientation of the stretching (θ) constant, and (3) not allowing rotation between scales ($e = 0$). Here, however, all four parameters were retrieved from the simulated events to compare their values against the parameter values identified for the observed event. This allowed exploring how good an approximation of the observed anisotropy can be achieved with the selected single-variable model calibration.

4.4. Effect of Anisotropy on Catchment-Scale Rainfall Accumulations

To produce estimates of rain events at the catchment scale in a computationally efficient way, the Bunyip River catchment was used as a mask, arranged in a regular grid at 25 locations over the rain field (see Figure 6 for placement of the catchments). The storms from the ensembles were sampled at each of these locations to create a total of 25000 catchment rain events per ensemble.

Due to some undesirable edge effects causing nonhomogeneous accumulation fields, explained in more detail in sections 5.3 and 5.7, the distributions of event accumulations at each location were studied. The mean event accumulations between the anisotropic and the isotropic model at each location were compared and a two-sample *t* test was used to assess the significance of the difference. Furthermore, the differences in the distributions were studied using the Kolmogorov-Smirnov test and the quantile test [*Johnson et al*., 1987], a nonparametric test specifically suited to detect a shift in a proportion of one population as compared to another.

4.5. Subsampling to Control Rainfall Accumulation

To facilitate further analysis, a subsample of 100 members from both ensembles was selected that produced the catchment accumulation closest to that of the observed event over the Bunyip River catchment ($P = 57.4$ mm). This allowed a more reliable comparison of the differences in the catchment precipitation properties and in the streamflow response between the anisotropic and isotropic events, by controlling for the fact that, all else being equal, higher rainfall results in higher runoff. Second, it allowed a comparison of the ability of both models to imitate the properties of the observed event at the catchment scale. To avoid spurious spatial correlation between members of the subsample, it was ensured that each subsample included no more than one catchment placement from each of the 1000 radar-scale storms.

The resulting subsamples were further refined such that they corresponded to the truncated conditional distribution:

$$Pr\left(P|P_{\min} \leq P \leq P_{\max}\right) \tag{11}$$

where P is the catchment accumulation, and P_{min} (52.7 mm) and P_{max} (61.7 mm) were calculated as the maximum lowest and the minimum highest values across the isotropic and anisotropic subsamples. In practice, the range of P was larger for isotropic storms than anisotropic storms, such that it was the anisotropic subsample that decided both limits. This resulted in 100 members in the anisotropic ensemble, and 40 members in the isotropic ensemble. It was considered computationally prohibitive to increase the isotropic ensemble sample size, given that 25000 catchment simulations only yielded 40 suitable samples (0.16%). The distributions of catchment accumulations between the subsampled ensembles were compared using the Kolmogorov-Smirnov test to ensure that they were not statistically different (p-value 0.465). This allowed for using these subsamples to further study other properties of rainfall events as well as the properties of streamflow at the catchment scale.

4.6. Effect of Anisotropy on Rainfall Temporal Distribution

The differences in the catchment storm hyetographs between anisotropic and isotropic ensembles were studied based on the probability distributions of the subsampled catchment rainfall events. The Kolmogorov-Smirnov test was used to compare the significance of difference in: (1) the fraction of wet time steps (WTS), (2) the average wet time step rain rate (R_{wet}), and (3) the maximum wet spell duration (WSD_{max}). A time step was considered wet if the catchment mean areal intensity exceeded 0.1 mm/h.

In addition, the Kolmogorov-Smirnov test and the quantile test for each of the descriptors were repeated for all the catchment locations using the full 1000 member ensembles of anisotropic and isotropic precipitation events.

Furthermore, the temporal autocorrelation functions (ACF) for both subsampled ensembles were calculated and compared to the ACF of the observed event.

4.7. Effect of Anisotropy on Streamflow Properties

The calibrated URBS model was run using the ensembles of subsampled catchment rainfall events as an input to observe whether the effects of anisotropy could be detected in the simulated streamflow. The rainfall fields were resampled for each of the subareas used in URBS as the area weighted averages of the radar cells contributing into each subarea. This gave a spatially uniform and temporally varying rainfall timeseries for each of the 56 subareas. As an initial condition, the catchment interception storage was set saturated and the infiltration storage nearly dry, roughly corresponding to observed catchment conditions at the time of the event. The stream network was set to be in dry state with no flow, since no comparisons with the observed streamflow hydrograph were required. The Tarago reservoir in the upper parts of the catchment was set to be full to prevent it from affecting the streamflow production by acting as an added storage.

The probability distributions of three flood event descriptors were compared between the anisotropic and isotropic ensembles at the catchment outlet and the significance of difference was studied using the Kolmogorov-Smirnov test. The studied flood event descriptors were: (1) the peak discharge (Q_p), (2) the flood volume (V), and (3) the time to peak (T_p). T_p was defined as the time from the centroid of the hyetograph to the time of the peak flow.

5. Results and Discussion

5.1. Evaluation of Model Calibration

The observed spatial scaling was reproduced appropriately by both models. The ensemble average power spectrum of both models closely followed the power spectrum of the observed event (Figure 3a). The temporal autocorrelation of the simulated mean areal rainfall over the entire field, measuring the goodness of the broken line model performance, was very close to the observed autocorrelation for both models up to lag times of 3 h (Figure 3b). At longer lags, the model autocorrelations did not follow the observed one but were still similar to each other. The models also struggled to reproduce the ensemble average Eulerian temporal correlations calculated at each pixel and averaged over the field (Figure 3c). The correlations were constantly slightly underestimated by both models except for the shortest lags. The anisotropic model performed slightly better than the isotropic model. This was the case even after attempts to increase the

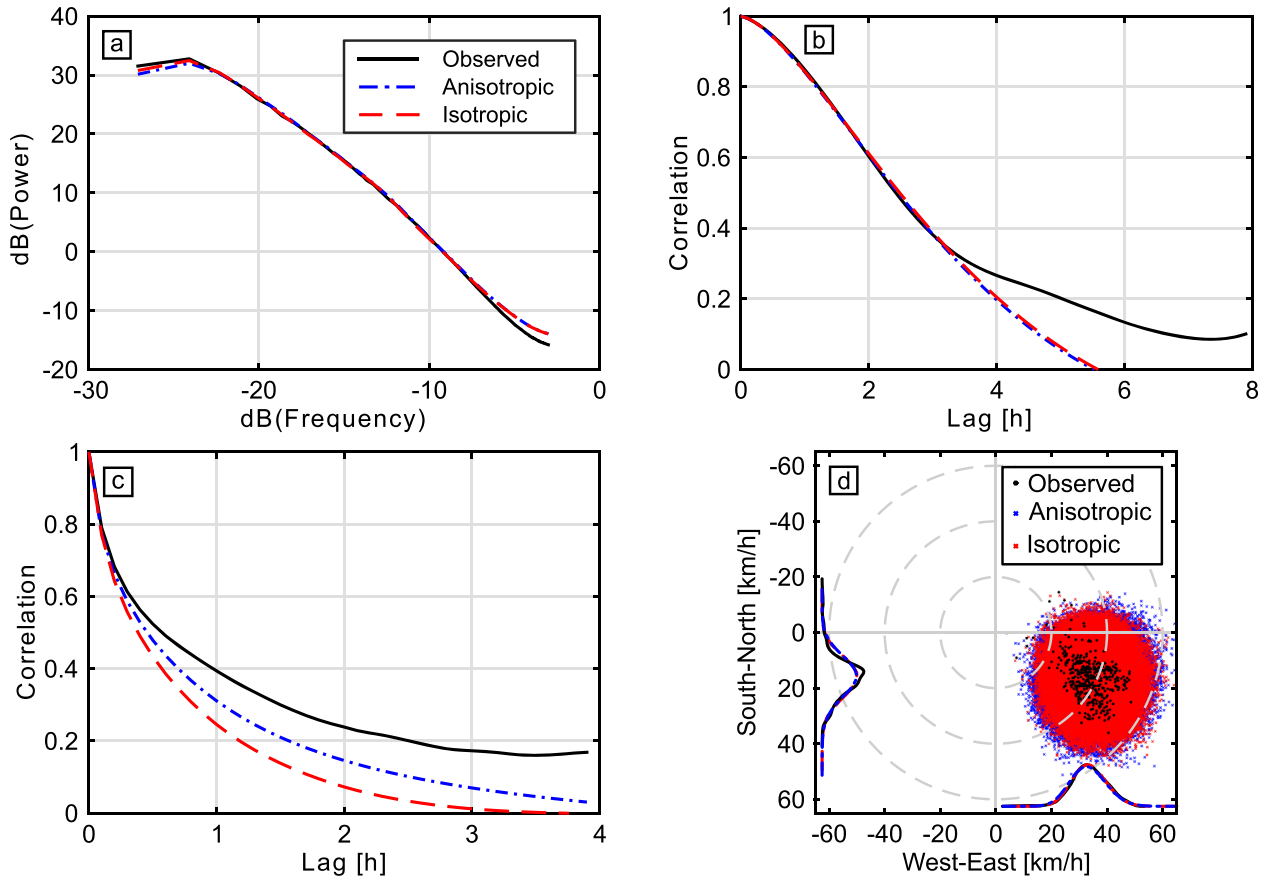

Figure 3. Evaluation of model calibration. Ensemble average (a) radially averaged spatial power spectrum, (b) temporal autocorrelation function of the mean areal rainfall, and (c) field-averaged Eulerian temporal autocorrelation function of the instantaneous rain fields at 1 km^2 pixel scale. (d) Advection velocities to southern and eastern directions for all the time steps of the ensemble members. Marginal distributions of the velocities are also presented.

temporal correlations of the isotropic model in the calibration phase by decreasing the advection velocities and altering the AR-model parameters. Both models were able to reproduce the observed mean and variance of the advection velocity time series toward the south and east. However, since the north-south and east-west advection velocity time series were modeled as two independent processes rather than as a bivariate process, the overall variance for both magnitude and direction of the advection was larger in the simulations than it was for the observed event (Figure 3d).

The distribution of the mean field accumulations was also evaluated. The distribution is expected to be the same for both isotropic and anisotropic models, as the precipitation model is essentially only a disaggregation model, distributing the given mean field reflectivity in space and time. The two-tailed Kolmogorov-Smirnov test (p-value 0.258) and the two-tailed two-sample t test (p-value 0.171) supported the null hypotheses that (1) the mean field accumulations produced by anisotropic and isotropic models follow the same probability distribution, and (2) that those distributions have the same mean value. Therefore, the shape (i.e., anisotropy) of the precipitation fields did not have a statistically significant effect on the mean field accumulations.

5.2. Evaluation of Anisotropy Simulation

For this paper's purposes, the anisotropic model had sufficient skill in creating fields with an elongated shape. As an example, two fields with identical field mean, field variance, and *WAR* are shown in Figure 4. The fields were generated using identical input noise field but with different power law and band-pass filters. Animations presenting the entire anisotropic and isotropic events of Figure 4 are provided in supporting information. Note that identical noise fields are only used here for illustration; in simulations the input noise fields for anisotropic and isotropic ensemble members were independent of each other.

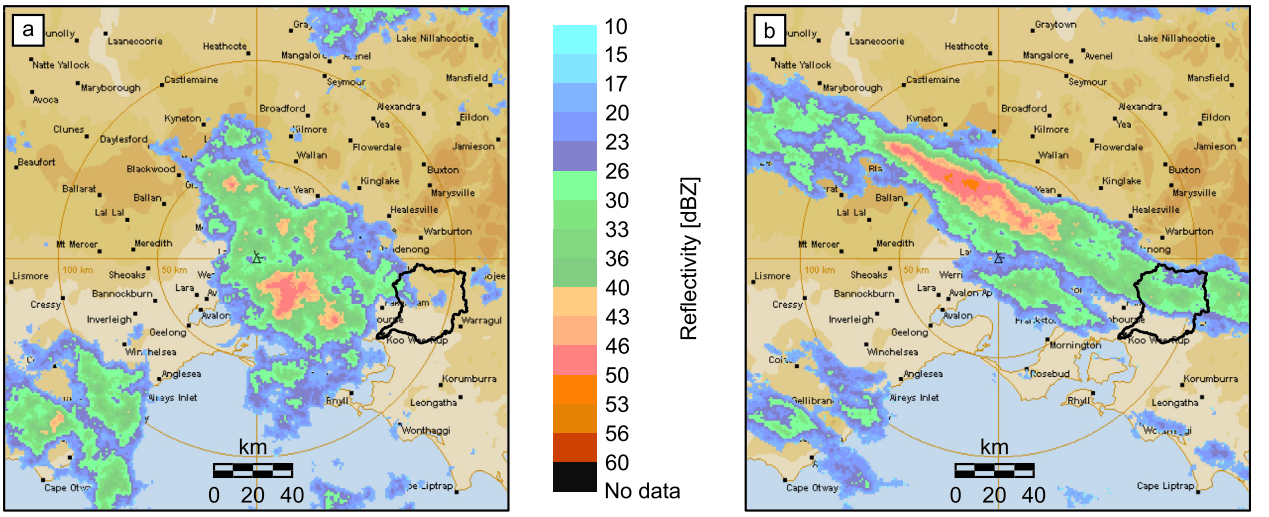

Figure 4. An example of a generated reflectivity field with (a) isotropic and (b) anisotropic shape. Other than the shape the fields have the same input parameters and for demonstration purposes, they also use the same stochastic noise as an input.

Figure 5 shows the cumulative distribution function (CDF) of r and θ estimated from and averaged across the 100 members from anisotropic and isotropic ensembles compared with the CDF calculated for the observed event. In addition, the time series of parameter estimates for observed data (r and θ) are

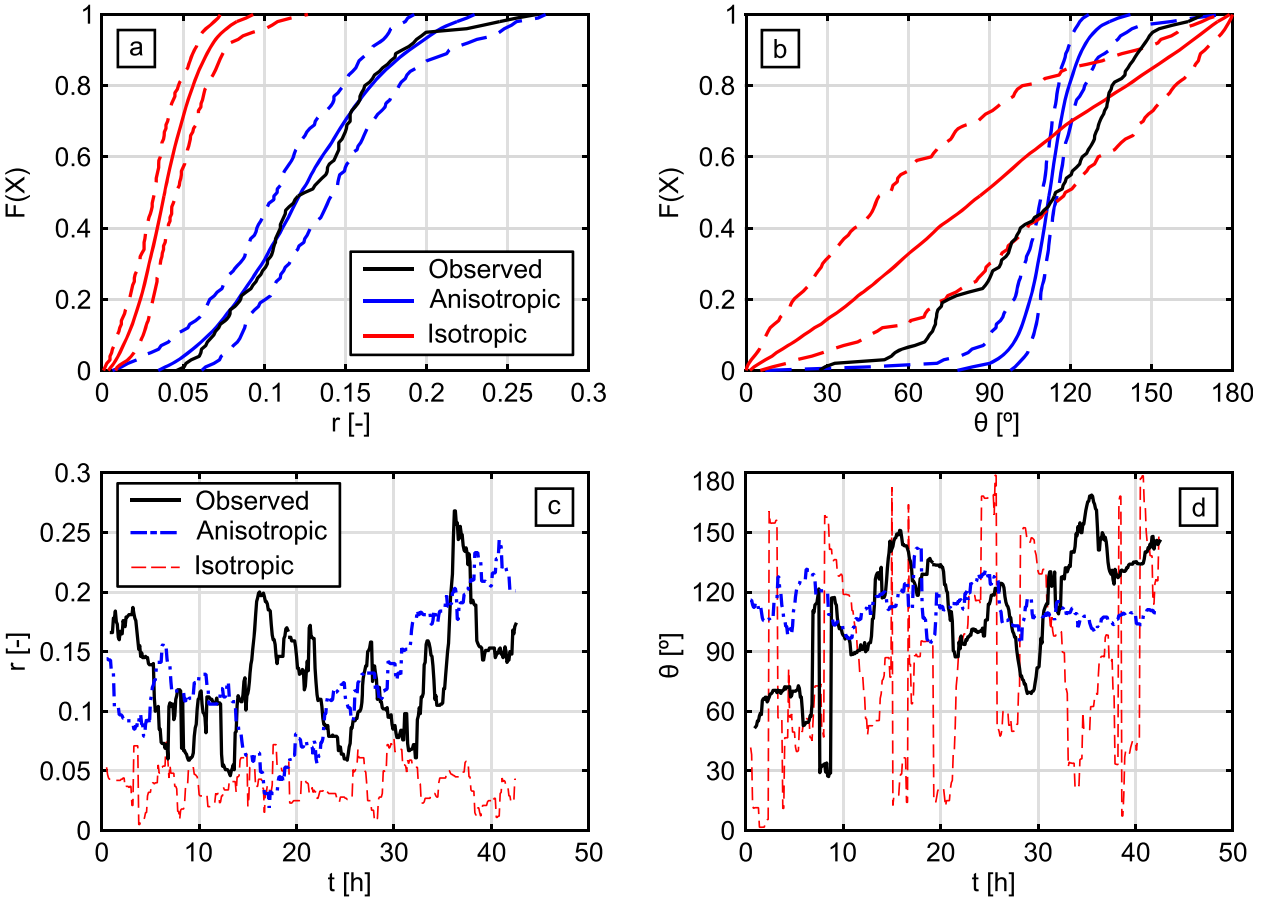

Figure 5. Ensemble average distributions of GSI parameters (a) r and (b) θ. Example time series for (c) r and (d) θ. Confidence bands (dashed lines) in (a) and (b) stand for 5th and 95th percentile around the mean values.

Table 1. Estimated Average GSI Parameter Values for the Observed Event and the Ensemble Average Values for 100 Simulation Members[a]

		Observed	Anisotropic	Isotropic
r		0.128 (0.046)	0.125 (0.046)	0.040 (0.019)
e		0.144 (0.259)	0.005 (0.174)	
θ	(°)	109.4 (31.4)	112.2 (10.2)	
l_s	(km)	5.8 (24.3)	3.2 (3.7)	

[a]Values in parentheses are the standard deviations around the average values.

presented together with example time series of simulated anisotropic and isotropic ensemble members. θ is presented as the compass bearing of the orientation, or elongation, of the rainband, between [0°,180°[such that 0° refers to the north and 90° to the east. Table 1 shows the estimated average values of r, θ, e, and l_s for the observed event and the selected anisotropic and isotropic ensemble members.

The anisotropic model captured well the range of the extent of stretching (r) of the system and the general variation of r in time but struggled to reproduce the more rapid changes. The ensemble average θ was close to the input value but there was less variation in the anisotropy orientation among the ensemble members than in the observed event due to the decision to keep it constant in time. On average, there was no rotation between the scales (e close to zero) for the anisotropic ensemble members, however, the variation in e for individual fields was large. This variation was discovered to be related to estimates of θ, so that e had a greater absolute value the further θ was estimated from its expected value. The decision to restrict the value of e to zero created a small discrepancy between the estimated ensemble average e for the simulations and the observed value, but it was justified already during the calibration process to be negligible. l_s was estimated to be constantly near the smallest scales for all the studied ensemble members. Based on the parameter estimates for the studied ensemble members, the anisotropic model as a whole gave reasonable estimates of the observed anisotropy at the radar scale using just r as a variable while keeping θ, e, and l_s constant.

The isotropic model simulations, as expected, showed only minor anisotropy in the generated fields. Estimated values of r rarely exceeded 0.1 and the anisotropy had no preferred orientation. The minor anisotropy is due to the stochastic noise used to create the precipitation fields, which does not produce perfectly circular precipitation features but roundish features with random orientations. The intermittent nature of the rain fields exaggerates the impression of anisotropy especially at large scales. Consider a field consisting of two separate isotropic features surrounded by dry areas; while the field appears isotropic at scales up to the feature size, at larger scales the field seems anisotropic as both features are visible. Parameters θ, e, and l_s have no discernible effect on the generated stochastic storms in isotropic situations where r is close to zero.

5.3. Effect of Anisotropy on Catchment-Scale Rainfall Accumulations

Figure 6 compares the properties of the generated catchment-scale rainfall accumulations for the anisotropic and isotropic models at the 25 studied locations over the rain field based on the 1000 member ensembles sampled at each location.

Considering first the ensemble average catchment rainfall accumulations, the isotropic model tends to produce higher accumulations near the corners and sides of the field and lower accumulations at the center of the field (Figure 6b). For the anisotropic model, the behavior is similar but the highest accumulations are in the NE and SW corners of the field, the NW and SE corners receiving less rain but still more than the center of the field (Figure 6a). Due to the disaggregation nature of the precipitation model, the expected mean accumulated rainfall at every catchment location and between the anisotropic and isotropic ensembles should be the same. While for most locations the anisotropic model produced slightly higher average accumulations than the isotropic model (Figure 6c), the differences were too small to be statistically significant according to the two-sample t test (Figure 6d). The models are thus giving expected results locally at the catchment locations, even though the accumulations are not homogenous over the entire field.

As the Bunyip River catchment is relatively small compared to the radar field, the differences in the spatial distribution of accumulation inside individual catchments were not large, and therefore were not considered problematic for closer catchment rainfall analysis. However, for a larger catchment, the nonhomogeneous accumulations within the catchment area could pose a serious challenge. The reasons and possible solutions to the nonhomogeneous accumulations are discussed later in section 5.7.

While the ensemble average catchment-scale rainfall accumulations are approximately the same between the anisotropic and isotropic ensembles for majority of the locations (Figures 6c and 6d), the distributions of those catchment accumulations are expected to differ. Since the elongation of the anisotropic structures

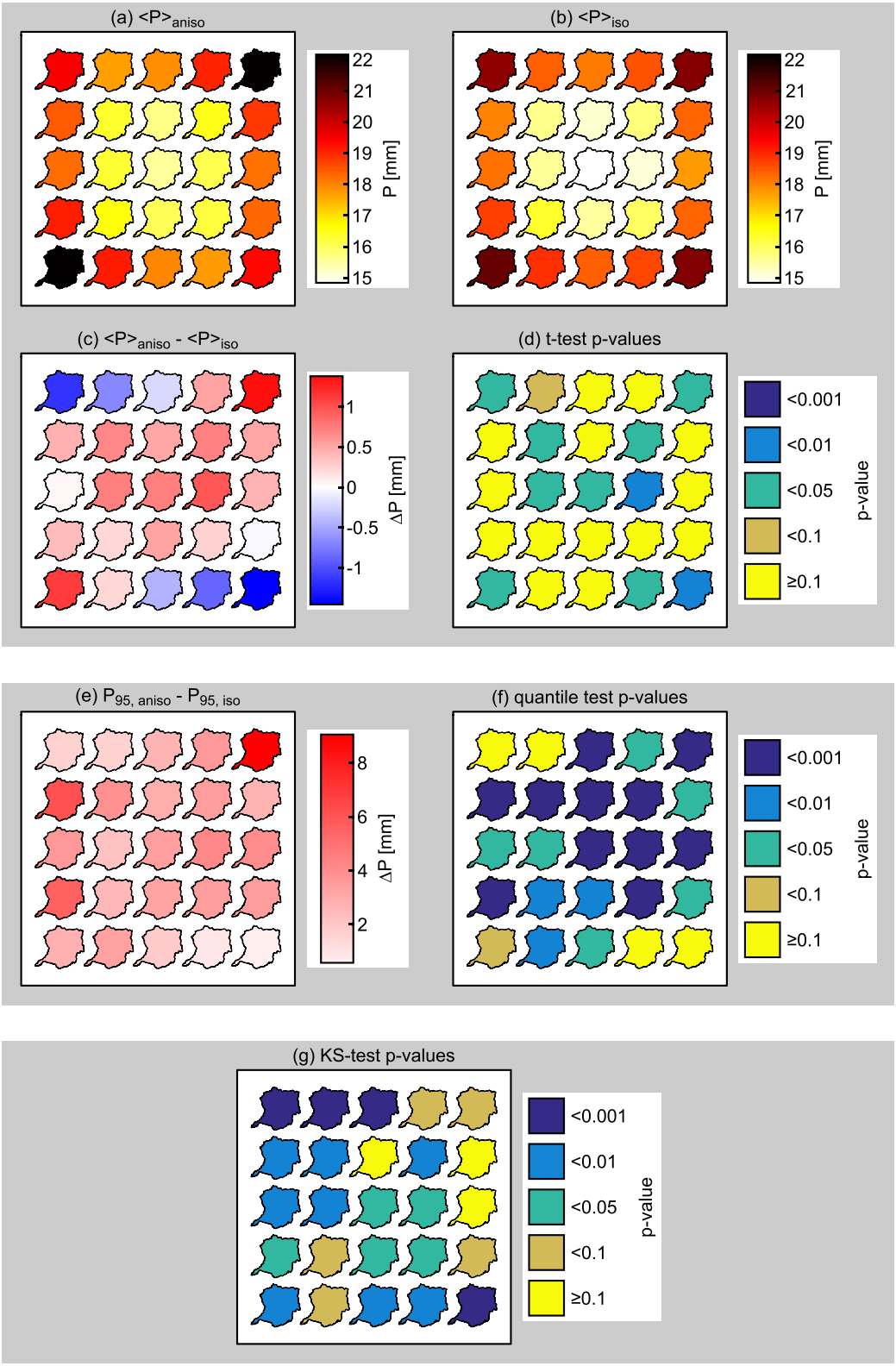

Figure 6. Catchment accumulation statistics at every catchment location. Ensemble average catchment accumulations for (a) anisotropic and (b) isotropic model for the 1000 ensemble members. (c) Differences in the ensemble average catchment accumulations and (d) test results of the two-sample *t* test for the significance of difference under the null hypothesis that the distributions have the same mean. (e) Differences in the 95th percentiles of catchment accumulation distributions and (f) test results of the quantile test for the significance of difference under the null hypothesis that the two distributions are the same with no difference in the 95th percentile. (g) Test results of the Kolmogorov-Smirnov test for the significance of difference in the accumulation distributions under the null hypothesis that the two distributions are the same.

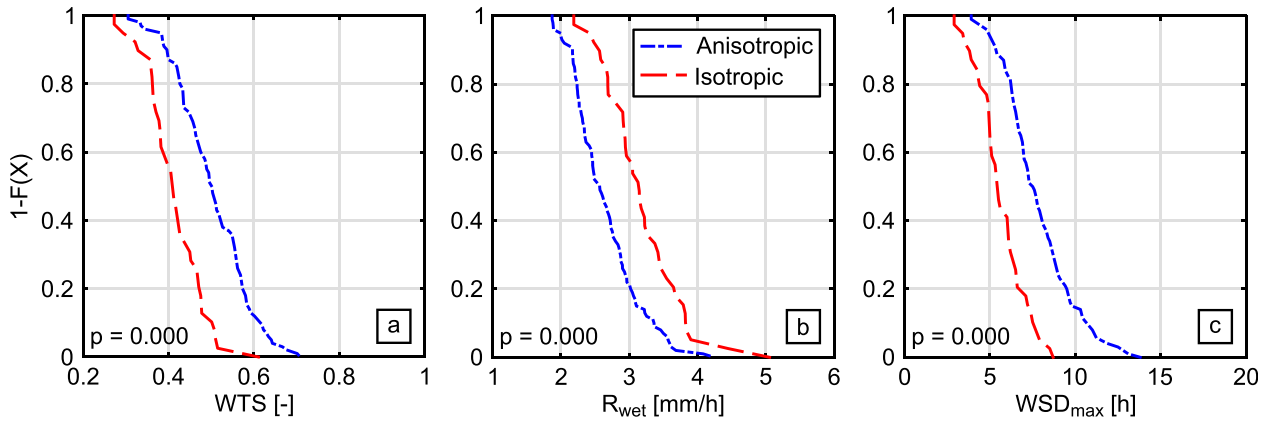

Figure 7. Distributions of (a) the fraction of wet time steps, (b) the average wet time step rain rate, (c) the maximum wet spell duration. *p*-values of the Kolmogorov-Smirnov test are shown under the null hypothesis that the studied descriptors in Figures 7a–7c follow the same probability distribution.

was almost parallel to the advection direction, it takes a longer time for an anisotropic precipitation feature to move over the catchment than for an otherwise identical, but isotropic, feature. Therefore, the anisotropic model should be more likely to generate high accumulations than the isotropic model. Similarly, the likelihood of an anisotropic feature missing the catchment due to its narrower shape is higher, which should be visible as a greater number of low accumulations in the anisotropic ensemble. Despite the decreased advection velocities for the isotropic model, the difference in the probability distributions of accumulated rainfall between the anisotropic and isotropic ensembles was confirmed to be statistically significant for most catchment locations using the Kolmogorov-Smirnov test (Figure 6g). Moreover, the quantile test for the significance of difference in the 95th percentile of the distributions confirmed the capability of the anisotropic model to create high accumulations more frequently than the isotropic model at almost every catchment location (Figures 6e and 6f). This was particularly clear when selecting the subsample with rainfall accumulation similar to the observed (extreme) event. Within the selected rainfall bounds, the anisotropic model generated 100 events, while the isotropic model only generated 40 events.

5.4. Effect of Anisotropy on Rainfall Temporal Distribution

Figure 7 presents the distributions for the studied descriptors of the catchment hyetographs and the *p*-values of the Kolmogorov-Smirnov test for the assumption that the descriptors follow the same distribution. The results support the hypothesis of the distributions being different.

The distributions of *WTS* (fraction of wet time steps) confirmed that the anisotropic model is capable of creating more wet time steps than the isotropic model. According to the distributions of WSD_{max} (maximum wet spell duration), the wet time steps of anisotropic events are more likely to follow each other, making the anisotropic storms last longer over the catchment than the isotropic storms. In order for the isotropic model to create as high accumulations as the anisotropic model, the lower *WTS* must be compensated by higher R_{wet} (average wet time step rain rate).

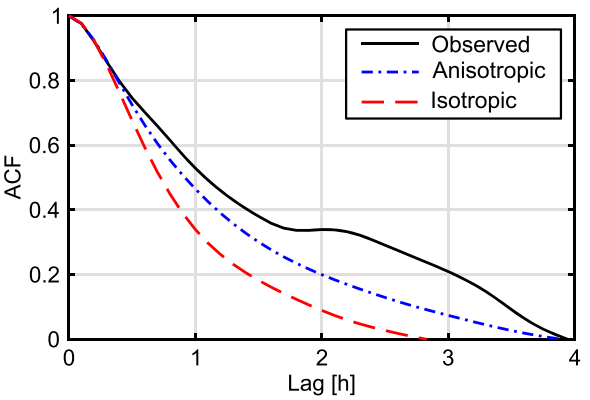

Figure 8. Ensemble-average temporal autocorrelation functions (ACF) of the subsampled catchment rainfall events and the ACF of the observed event.

These results were not significantly affected by the nonhomogeneous accumulations at the radar scale. Regardless of the catchment location, the difference in the distributions of *WTS* and WSD_{max} computed for the 1000 member ensembles of anisotropic and isotropic storms was strongly statistically significant ($p < 0.001$) according to the Kolmogorov-Smirnov test and the quantile test. In other words, the anisotropic model

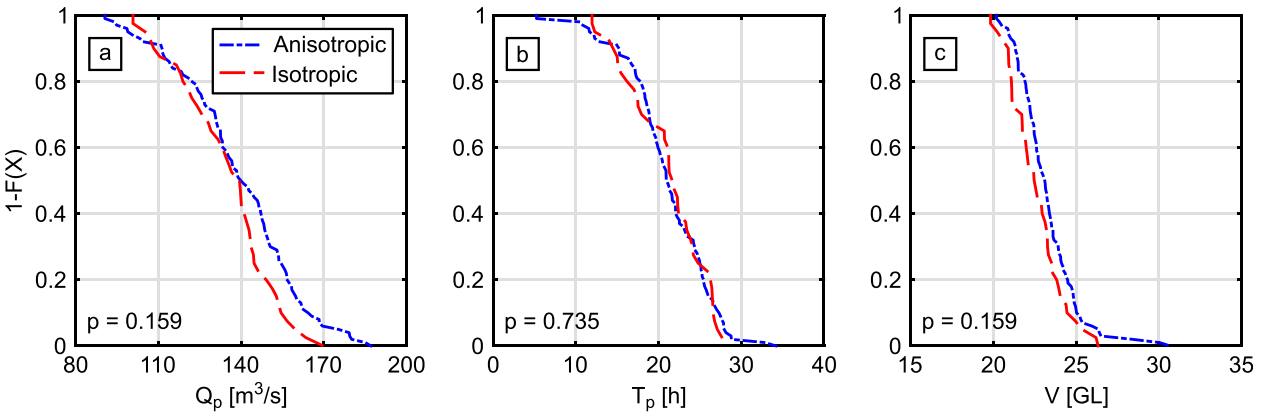

Figure 9. Distributions of (a) peak flow, (b) time to peak, and (c) flood volume. *p*-values of the Kolmogorov-Smirnov test are shown under the null hypothesis that the studied descriptors in Figures 9a–9c follow the same probability distribution.

produced more high values and hence longer lasting storms than the isotropic model. The difference in the distributions of R_{wet} was statistically significant ($p < 0.05$) for most locations, with the median of the isotropic distribution generally shifted right from the median of the anisotropic distribution.

Figure 8 shows the catchment-scale temporal autocorrelation functions (ACF) averaged across the subsampled rainfall events. As the elongation of the anisotropic features was almost parallel to the direction of advection, it takes a longer time for an anisotropic storm to move over the catchment compared to an otherwise equal but isotropic storm. Therefore, on average, the anisotropic storms should result in higher temporal correlations of rainfall intensities over the catchment. Accordingly, in Figure 8, the anisotropic model showed greater skill than the isotropic model in reproducing the observed catchment-scale ACF. This result occurs despite the isotropic model being deliberately calibrated to improve its skill at reproducing temporal autocorrelation. As with radar-scale results, both models still underestimate the observed catchment-scale ACF, notably for lags greater than half an hour. However, this result suggests that capturing anisotropy helps to generate storms similar to the observed event.

5.5. Effect of Anisotropy on Streamflow Properties

Keeping catchment rainfall accumulation (approximately) constant, the anisotropy only had a minor impact on the streamflow response as the distributions of all the studied streamflow descriptors were very similar for anisotropic and isotropic rainfall ensembles (Figure 9). Especially T_p (time to peak) was insensitive to the anisotropy of the fields. The anisotropic precipitation fields resulted in marginally higher Q_p (peak flow) and V (flood volume) than the isotropic fields, but these differences were too small to be statistically significant according to the Kolmogorov-Smirnov test. The lack of statistical significance could however be influenced by the computationally restricted small sample size.

If the analysis did not control for rainfall accumulation P, results (not shown) confirmed that there is a strong connection between P and Q_p, as well as between P and V. Therefore, in general the anisotropic model is capable of creating more severe floods more frequently than the isotropic model simply because it is more likely to create high catchment accumulations.

5.6. Factors Influencing Effect of Anisotropy on Streamflow Properties

The results for streamflow response are somewhat surprising as little difference was detected between the anisotropic and isotropic rainfall fields especially for T_p. Yet previously e.g., *Beven and Hornberger* [1982] and *Singh* [1997] have noticed the spatial variability of rainfall to particularly affect the timing of the runoff hydrograph, with less impact on the peak flow and the flow volume. Typically the focus in the earlier research has been in comparing spatially varying and spatially uniform rainfall. Here, when URBS simulations were repeated using spatially uniform rainfall input, only minor differences in stream flow response were noticed to spatially varying input. This confirms the rainfall-runoff model being rather insensitive to the spatial structure of rainfall at the catchment scale. Also, due to the small size of the Bunyip River catchment relative to the size of the precipitation structures, the anisotropic and isotropic precipitation features may appear spatially very similar from the catchment perspective regardless of their large-scale shape.

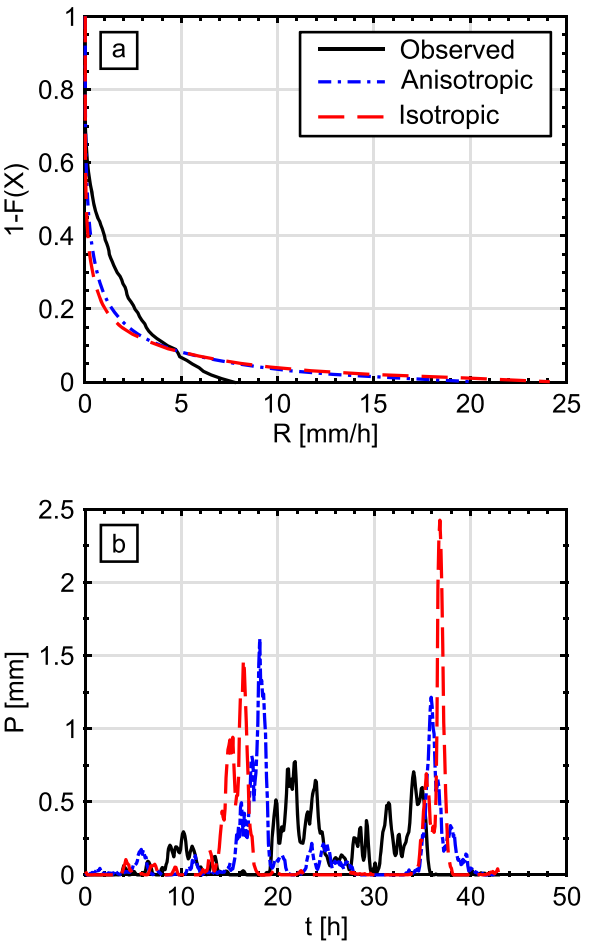

Figure 10. (a) Ensemble average exceedance probabilities of catchment rainfall intensities for individual time steps of the subsampled ensembles, and (b) example time series of catchment rainfall time series.

The dampening effect of rural catchments has led several researchers to suggest that an accurate estimation of the volume of water input, rather than its spatial structure, is the dominating factor affecting the streamflow response [*Beven and Hornberger*, 1982; *Obled et al.*, 1994; *Nicótina et al.*, 2008]. This is in accordance with the results obtained here since controlling for accumulation eliminated significant differences between streamflow properties of anisotropic and isotropic ensembles. The dampening effect has been noticed to increase with the catchment size [e.g., *Skøien and Blöschl*, 2006; *Segond et al.*, 2007; *Mandapaka et al.*, 2009], which has led *Pokhrel and Gupta* [2011] to suggest studying the streamflow properties at a number of locations along the stream and not just at the catchment outlet. However, when the ensemble distributions of the hydrograph properties were studied at the scale of URBS subcatchments, the results (not shown) did not reveal greater differences than what was observed at the catchment scale.

An abundance of literature has related the direction and magnitude of storm advection to the streamflow response, with a general consensus that storms moving in downstream direction generate higher peak flow and more varying hydrograph shapes than upstream moving storms [*Singh*, 1997; *de Lima and Singh*, 2002; *Lee and Huang*, 2007], although some studies have shown no relation between storm movement and flood response [e.g., *Nikolopoulos et al.*, 2014]. In addition, *de Lima and Singh* [2002] noticed that the sensitivity of runoff to storm patterns decreases at high storm speeds. Here, however, such impacts were not investigated, since the focus was on an observed limit case having the storm advection approximately perpendicular to the general stream flow direction and parallel to the elongation of the anisotropic features.

Regarding the rainfall-runoff model, the role of the initial moisture status of the catchment in shaping the runoff response has been emphasized in previous research [e.g., *Shah et al.*, 1996; *Fenicia et al.*, 2008; *Paschalis et al.*, 2014]. Here, the effect of the initial soil moisture was studied by repeating the URBS simulations after changing the initial infiltration storage status in the model from nearly empty to nearly full. As expected, increase in the values of Q_p and V was observed due to greater amount of precipitation contributing to surface flow instead of being reserved in the subsurface storage. However, the changes were negligible in terms of differences between the ensembles of anisotropic and isotropic design events.

The precipitation fields were generated using a spatial resolution of 1 km^2, but subsequently the high-resolution fields were resampled into 56 spatially uniform subareal time series for URBS. This diminishes the advantage of having rainfall input with a high spatial resolution, and has been criticized before by *Yu et al.* [2005]. Here the subareas were mainly relatively small (average 19.5 km^2), with a spatial scale ($\sim$ 5 km) relatively close to the sphero-scale of the anisotropic fields (2 km). The anisotropic structures at the scale of a subarea are therefore also nearly isotropic, such that it is the large-scale anisotropy of the fields that is expected to most affect the catchment response. The distortion due to the subareal averaging is likely to have a minimal effect on the results when comparing discharge values generated by anisotropic and isotropic storms, even if it does affect the discharge predictions themselves [e.g., *Nikolopoulos et al.*, 2011].

A closer look was taken at the precipitation time series over the catchment to explain the similarity of the streamflow results. First, ensemble average exceedance probabilities were calculated for the precipitation intensities over all time steps (Figure 10a), and the probability distributions were noticed to be quite similar for both subsampled ensembles. Moreover, irrespective of the ensemble, they both had too few intermediate and too many high intensity values when compared to the observed event. Example time series corresponding to individual ensemble members generated by the models support this observation (Figure 10b). Even though the anisotropic model was capable of producing catchment rain events with longer duration of continuous rainfall than the isotropic model, high rainfall accumulations for both models typically resulted from very high-intensity rain cells hitting the catchment for a short period of time. This contrasts with the observed event, in which the high accumulations arose from long durations of continuous but less intense rainfall.

5.7. Possible Solutions to Identified Issues

Two main problems were identified regarding the results. First, at radar scale the field accumulations were noticed to be location dependent rather than homogeneous over the field. Second, at catchment scale the rainfall time series could not reliably reproduce the temporal properties of the observed event.

The nonhomogeneity in the field accumulations was presumed to result from the way the advection and the temporal development of the precipitation features were described in the model. The periodic nature of the Fourier transform (wrap-around) was utilized to simulate advection, i.e., the precipitation features were allowed to fold symmetrically around the edges of the field. Real precipitation features do not behave like this and therefore, as explained by *Bell* [1987], only a quarter of the field can be utilized without the symmetry becoming a problem. This study addressed the problem by creating noise fields four times the desired size of the final field and then trimmed them to the final size. However, due to the dynamic scaling scheme used in STEPS, the actual size required for the original noise fields also depends on the advection velocity and the temporal development of the fields. The fields need to be sufficiently large so that even the largest precipitation structures have time to evolve into new structures before the advection moves them across the field and they reappear from the opposite side of the field. Choosing the ideal size for the noise fields is not trivial, however, but becomes a compromise involving restricting the lifetime of the largest structures to prevent these nonhomogeneous accumulations, retaining acceptable temporal scaling structure in the model, and minimizing the computational expense of the model, which increases with field size.

While the focus here was on an individual extreme event, the obtained catchment-scale results highlight the difficulty of producing a catchment rainfall time series like the one observed over the Bunyip River catchment in February 2011. The precipitation event itself was exceptional, producing daily rainfall totals across the Melbourne Metropolitan area as large as what would typically be observed over the entire summer season. In addition, the Bunyip River catchment was badly affected as many of the thunderstorms developed one after another, moving almost directly over the catchment in a squall line formation. Even though the precipitation model yielded good results at the radar scale, reproducing such an extreme event for a region comprising only 2% of the radar field proved to be an extremely difficult task. The model relies on the scaling formalism in time and space, but it is clearly problematic to produce such extreme results at a much smaller scale than what was used in parameter estimation. However, estimating parameters on the smaller catchment scale would pose other challenges. The time series for the mean areal rainfall and its temporal scaling structure could be captured but the spatial aspects, and in particular the anisotropy estimation, require data also from larger scales. The spatial and spatiotemporal correlations also need an adequate number of data points for their reliable estimation, which calls for data from a sufficiently large region.

Improved temporal results at the catchment scale could be achieved by sacrificing realism of anisotropy at the radar scale in order to improve control of catchment-scale properties. Keeping the level of stretching (r) constant at a reasonably high value for the entire duration of the event would result in stronger forcing for banded precipitation features increasing the probability of creating continuous rainfall at the catchment scale.

6. Conclusions

The anisotropy encountered in precipitation fields has the potential to significantly affect the rainfall accumulation, depending on the orientation of the anisotropy in relation to the advection of the fields. To account for the anisotropy in design storm generation, a state-of-the-art precipitation generator STEPS was

combined with a linear approximation of the GSI formalism. As a case study, an observed extreme precipitation event was studied. The event had a distinct rainband form oriented nearly parallel to the storm advection, thus representing a hydrologically interesting limit case in which anisotropy is expected to have the most effect on catchment rainfall and discharge. This event was used to parameterize two models to create ensembles of isotropic and anisotropic design storms. The resulting ensembles were analyzed at radar and much smaller catchment scales, and they were subsequently routed through a rainfall-runoff model to study the differences in the simulated streamflow at the catchment outlet.

At the radar scale, accounting for anisotropy yielded precipitation fields that resembled the observed event more closely than those generated using the isotropic model, even though the anisotropy was described using only one variable. Both models were found to lead to nonhomogeneous accumulation fields, likely due to difficulties in simultaneously achieving persistence of temporal structures and continuous wrap-around advection. The resulting unevenly distributed rainfall was not problematic for this analysis due to the relatively small size of the studied catchment, but may be of concern for larger catchments.

At the catchment scale, the anisotropic model was more likely to create high accumulations than the isotropic model, with larger accumulations naturally translating into more severe floods. To achieve similar accumulations, the longer periods of rainfall generated by the anisotropic model were compensated in the isotropic model by increased rainfall intensities. The streamflow responses between those anisotropic and isotropic ensemble members that produced approximately same catchment accumulation were however similar, suggesting that anisotropy is less important than other factors affecting streamflow generation. In addition, the durations of continuous rain produced by the anisotropic model were still too short and the rainfall intensities too high when compared to the observed event. This may help explain the small differences in the streamflow response between the ensembles. It also highlights the extreme nature of the observed event and the difficulty of producing representative rain events at the catchment scale when the model is calibrated at the much larger radar scale.

The proposed combination of STEPS and linear GSI provides a tool to generate design storms with anisotropic characteristics, allowing description of more realistic precipitation features than what can be achieved with the commonly applied isotropic simulation models. The effect of spatial anisotropy was more prominent when addressing precipitation characteristics directly, but its effect was attenuated when exploring streamflow produced by storm events. Clearly, the factors influencing the effect of anisotropy are complex. The current study lays groundwork for future advances, notwithstanding its limitations in studying only one extreme case on a single catchment using an operational, but semidistributed, rainfall-runoff model. Accordingly, in future research it is suggested to study the impact of precipitation field anisotropy to stream flow generation using a fully distributed model in different catchment settings with a set of precipitation events having varying degrees of anisotropy.

Acknowledgments
We gratefully acknowledge the funding provided for the first author by Maa- ja Vesitekniikan tuki ry. We would like to thank the Australian Government Bureau of Meteorology for providing the precipitation data for Melbourne region, Melbourne Water for providing the data regarding the Bunyip River catchment, and Don Carroll for help with the URBS model. We thank Pierluigi Furcolo and the two anonymous reviewers, as well as the associate editor for their helpful and constructive comments. Contact the corresponding author to request the data used in this study.

References

Bell, T. L. (1987), A space-time stochastic model of rainfall for satellite remote-sensing studies, *J. Geophys. Res.*, *92*(D8), 9631–9643, doi:10.1029/JD092iD08p09631.

Beven, K. J., and G. M. Hornberger (1982), Assessing the effect of spatial pattern of precipitation in modeling stream flow hydrographs, *J. Am. Water Resour. Assoc.*, *18*(5), 823–829, doi:10.1111/j.1752-1688.1982.tb00078.x.

Bowler, N. E. H., C. E. Pierce, and A. Seed (2004), Development of a precipitation nowcasting algorithm based upon optical flow techniques, *J. Hydrol.*, *288*(1–2), 74–91, doi:10.1016/j.jhydrol.2003.11.011.

Bowler, N. E., C. E. Pierce, and A. W. Seed (2006), STEPS: A probabilistic precipitation forecasting scheme which merges an extrapolation nowcast with downscaled NWP, *Q. J. R. Meteorol. Soc.*, *132*(620), 2127–2155, doi:10.1256/qj.04.100.

Carroll, D. G. (1998), URBS: a catchment management and flood forecasting rainfall runoff routing model, Brisbane City Council, Brisbane, Qld.

Charalambous, J., A. Rahman, and D. Carroll (2013), Application of Monte Carlo simulation technique to design flood estimation: A case study for north Johnstone River in Queensland, Australia, *Water Resour. Manage.*, *27*(11), 4099–4111, doi:10.1007/s11269-013-0398-9.

de Lima, J. L. M. P., and V. P. Singh (2002), The influence of the pattern of moving rainstorms on overland flow, *Adv. Water Resour.*, *25*(7), 817–828, doi:10.1016/S0309-1708(02)00067-2.

De Michele, C., and P. Bernardara (2005), Spectral analysis and modeling of space-time rainfall fields, *Atmos. Res.*, *77*(1–4), 124–136, doi:10.1016/j.atmosres.2004.10.031.

Doherty, J. (2010), PEST: Model-Independent Parameter Estimation, User Manual, 5th ed., Watermark Numer. Comput. [Available at http://www.pesthomepage.org/Downloads.php.]

Ebtehaj, M., and E. Foufoula-Georgiou (2010), Orographic signature on multiscale statistics of extreme rainfall: A storm-scale study, *J. Geophys. Res.*, *115*, D23112, doi:10.1029/2010JD014093.

Fenicia, F., H. H. G. Savenije, P. Matgen, and L. Pfister (2008), Understanding catchment behavior through stepwise model concept improvement, *Water Resour. Res.*, *44*, W01402, doi:10.1029/2006WR005563.

Gabellani, S., G. Boni, L. Ferraris, J. von Hardenberg, and A. Provenzale (2007), Propagation of uncertainty from rainfall to runoff: A case study with a stochastic rainfall generator, *Adv. Water Resour.*, *30*(10), 2061–2071, doi:10.1016/j.advwatres.2006.11.015.
Gires, A., C. Onof, C. Maksimovic, D. Schertzer, I. Tchiguirinskaia, and N. Simoes (2012), Quantifying the impact of small scale unmeasured rainfall variability on urban runoff through multifractal downscaling: A case study, *J. Hydrol.*, *442-443*, 117–128, doi:10.1016/j.jhydrol.2012.04.005.
Johnson, R. A., S. Verrill, and D. H. Moore II (1987), Two-sample rank tests for detecting changes that occur in a small proportion of the treated population, *Biometrics*, *43*(3), 641–655, doi:10.2307/2532001.
Kumar, P., and E. Foufoula-Georgiou (1993), A new look at rainfall fluctuations and scaling properties of spatial rainfall using orthogonal wavelets, *J. Appl. Meteorol.*, *32*(2), 209–222, doi:10.1175/1520-0450(1993)032 < 0209:ANLARF>2.0.CO;2.
Leblois, E., and J.-D. Creutin (2013), Space-time simulation of intermittent rainfall with prescribed advection field: Adaptation of the turning band method, *Water Resour. Res.*, *49*, 3375–3387, doi:10.1002/wrcr.20190.
Lee, K. T., and J.-K. Huang (2007), Effect of moving storms on attainment of equilibrium discharge, *Hydrol. Processes*, *21*(24), 3357–3366, doi:10.1002/hyp.6548.
Lovejoy, S., and D. Schertzer (2013), *The Weather And Climate: Emergent Laws And Multifractal Cascades*, Cambridge Univ. Press, Cambridge.
Mandapaka, P. V., W. F. Krajewski, R. Mantilla, and V. K. Gupta (2009), Dissecting the effect of rainfall variability on the statistical structure of peak flows, *Adv. Water Resour.*, *32*(10), 1508–1525, doi:10.1016/j.advwatres.2009.07.005.
Marsan, D., D. Schertzer, and S. Lovejoy (1996), Causal space-time multifractal processes: Predictability and forecasting of rain fields, *J. Geophys. Res.*, *101*(D21), 26,333–26,346, doi:10.1029/96JD01840.
Mellor, D. (1996), The modified turning bands (MTB) model for space-time rainfall. I. Model definition and properties, *J. Hydrol.*, *175*(1–4), 113–127, doi:10.1016/S0022-1694(96)80008-4.
Nicótina, L., E. Alessi Celegon, A. Rinaldo, and M. Marani (2008), On the impact of rainfall patterns on the hydrologic response, *Water Resour. Res.*, *44*, W12401, doi:10.1029/2007WR006654.
Niemi, T. J., T. Kokkonen, and A. W. Seed (2014), A simple and effective method for quantifying spatial anisotropy of time series of precipitation fields, *Water Resour. Res.*, *50*, 5906–5925, doi:10.1002/2013WR015190.
Nikolopoulos, E. I., E. N. Anagnostou, M. Borga, E. R. Vivoni, and A. Papadopoulos (2011), Sensitivity of a mountain basin flash flood to initial wetness condition and rainfall variability, *J. Hydrol.*, *402*(3–4), 165–178, doi:10.1016/j.jhydrol.2010.12.020.
Nikolopoulos, E. I., M. Borga, D. Zoccatelli, and E. N. Anagnostou (2014), Catchment-scale storm velocity: Quantification, scale dependence and effect on flood response, *Hydrol. Sci. J.*, *59*(7), 1363–1376, doi:10.1080/02626667.2014.923889.
Northrop, P. (1998), A clustered spatial-temporal model of rainfall, *Proc. R. Soc. London Ser. A*, *454*(1975), 1875–1888, doi:10.1098/rspa.1998.0238.
Obled, C., J. Wendling, and K. Beven (1994), The sensitivity of hydrological models to spatial rainfall patterns: An evaluation using observed data, *J. Hydrol.*, *159*(1–4), 305–333, doi:10.1016/0022-1694(94)90263-1.
Paschalis, A., P. Molnar, S. Fatichi, and P. Burlando (2013), A stochastic model for high-resolution space-time precipitation simulation, *Water Resour. Res.*, *49*, 8400–8417, doi:10.1002/2013WR014437.
Paschalis, A., S. Fatichi, P. Molnar, S. Rimkus, and P. Burlando (2014), On the effects of small scale space–time variability of rainfall on basin flood response, *J. Hydrol.*, *514*, 313–327, doi:10.1016/j.jhydrol.2014.04.014.
Pecknold, S., S. Lovejoy, D. Schertzer, C. Hooge, and J. F. Malouin (1993), The simulation of universal multifractals, in *Cellular Automata: Prospects in Astrophysical Applications*, edited by J. M. Perdang and A. Lejeune, pp. 228–267, World Sci., Singapore.
Pegram, G. G. S., and A. N. Clothier (2001), High resolution space–time modelling of rainfall: The "String of Beads" model, *J. Hydrol.*, *241*(1–2), 26–41, doi:10.1016/S0022-1694(00)00373-5.
Pflug, K., S. Lovejoy, and D. Schertzer (1993), Differential rotation and cloud texture: Analysis using generalized scale invariance, *J. Atmos. Sci.*, *50*(4), 538–554, doi:10.1175/1520-0469(1993)050 < 0538:DRACTA>2.0.CO;2.
Pokhrel, P., and H. V. Gupta (2011), On the ability to infer spatial catchment variability using streamflow hydrographs, *Water Resour. Res.*, *47*, W08534, doi:10.1029/2010WR009873.
Rahman, A., D. Carroll, P. Mahbub, S. Khan, and K. Rahman (2007), Application of the URBS-Monte Carlo simulation technique to Urban catchments: A case study for the Coomera River Catchment in Gold Coast Australia, *Water Pract. Technol.*, *2*(2), 2014 pp., doi:10.2166/wpt.2007.0039.
Rebora, N., L. Ferraris, J. von Hardenberg, and A. Provenzale (2006), RainFARM: Rainfall downscaling by a filtered autoregressive model, *J. Hydrometeorol.*, *7*(4), 724–738, doi:10.1175/JHM517.1.
Schertzer, D., and S. Lovejoy (1985), Generalised scale invariance in turbulent phenomena, *Physicochem. Hydrodyn.*, *6*(5–6), 623–635.
Schleiss, M., S. Chamoun, and A. Berne (2014), Stochastic simulation of intermittent rainfall using the concept of "dry drift," *Water Resour. Res.*, *50*, 2329–2349, doi:10.1002/2013WR014641.
Seed, A. W., C. Draper, R. Srikanthan, and M. Menabde (2000), A multiplicative broken-line model for time series of mean areal rainfall, *Water Resour. Res.*, *36*(8), 2395–2399, doi:10.1029/2000WR900117.
Seed, A. W., C. E. Pierce, and K. Norman (2013), Formulation and evaluation of a scale decomposition-based stochastic precipitation nowcast scheme, *Water Resour. Res.*, *49*, 6624–6641, doi:10.1002/wrcr.20536.
Seed, A., P. Jordan, C. Pierce, M. Leonard, R. Nathan, and E. Kordomenidi (2014), Stochastic simulation of space-time rainfall patterns for the brisbane river catchment, in *Hydrology and Water Resources Symposium 2014*, pp. 1026–1039, Engineers Australia, Barton, A.C.T.
Segond, M.-L., H. S. Wheater, and C. Onof (2007), The significance of spatial rainfall representation for flood runoff estimation: A numerical evaluation based on the Lee catchment, UK, *J. Hydrol.*, *347*(1–2), 116–131, doi:10.1016/j.jhydrol.2007.09.040.
Shah, S. M. S., P. E. O'Connell, and J. R. M. Hosking (1996), Modelling the effects of spatial variability in rainfall on catchment response. 2. Experiments with distributed and lumped models, *J. Hydrol.*, *175*(1–4), 89–111, doi:10.1016/S0022-1694(96)80007-2.
Singh, V. P. (1997), Effect of spatial and temporal variability in rainfall and watershed characteristics on stream flow hydrograph, *Hydrol. Processes*, *11*(12), 1649–1669, doi:10.1002/(SICI)1099-1085(19971015)11:12 < 1649::AID-HYP495 > 3.0.CO;2-1.
Skøien, J. O., and G. Blöschl (2006), Catchments as space-time filters: A joint spatiotemporal geostatistical analysis of runoff and precipitation, *Hydrol. Earth Syst. Sci.*, *10*(5), 645–662, doi:10.5194/hess-10-645-2006.
Veneziano, D., A. Langousis, and P. Furcolo (2006), Multifractality and rainfall extremes: A review, *Water Resour. Res.*, *42*, W12401, doi:10.1029/2005WR004716.
Venugopal, V., E. Foufoula-Georgiou, and V. Sapozhnikov (1999), Evidence of dynamic scaling in space-time rainfall, *J. Geophys. Res.*, *104*(D24), 31,599–31,610, doi:10.1029/1999JD900437.
Vischel, T., T. Lebel, S. Massuel, and B. Cappelaere (2009), Conditional simulation schemes of rain fields and their application to rainfall–runoff modeling studies in the Sahel, *J. Hydrol.*, *375*(1–2), 273–286, doi:10.1016/j.jhydrol.2009.02.028.

Volpi, E., M. Di Lazzaro, and A. Fiori (2012), A simplified framework for assessing the impact of rainfall spatial variability on the hydrologic response, *Adv. Water Resour.*, *46*, 1–10, doi:10.1016/j.advwatres.2012.04.011.

Waymire, E., V. K. Gupta, and I. Rodriguez-Iturbe (1984), A spectral theory of rainfall intensity at the meso-β scale, *Water Resour. Res.*, *20*(10), 1453–1465, doi:10.1029/WR020i010p01453.

Willeit, M., R. Amorati, A. Montani, V. Pavan, and M. S. Tesini (2015), Comparison of spectral characteristics of precipitation from radar estimates and COSMO-model predicted fields, *Meteorol. Atmos. Phys.*, *127*(2), 191–203, doi:10.1007/s00703-014-0359-8.

Yu, B., A. Seed, L. Pu, and T. Malone (2005), Integration of weather radar data into a raster GIS framework for improved flood estimation, *Atmos. Sci. Lett.*, *6*(1), 66–70, doi:10.1002/asl.95.

Zawadzki, I. I. (1973), Statistical properties of precipitation patterns, *J. Appl. Meteorol.*, *12*(3), 459–472, doi:10.1175/1520-0450(1973)012 < 0459:SPOPP>2.0.CO;2.